



The role of latent heating in warm frontogenesis

Adele L. Igel* and Susan C. van den Heever

Colorado State University, Fort Collins, CO, USA

*Correspondence to: A. L. Igel, Department of Atmospheric Science, Colorado State University, 1371 Campus Delivery, Fort Collins, CO 80523, USA. E-mail: adele.igel@colostate.edu

The role of latent heating from individual cloud processes associated with one part of a springtime extratropical cyclone, the warm front, is assessed using high-resolution modelling. Condensation and cloud droplet nucleation are the largest sources of latent heat along the frontal surface and together produce rates of horizontal frontogenesis that are of the same order of magnitude as the deformation and tilting terms at mid levels; however, near the surface latent heating does not cause strong frontogenesis. In the vertical, stabilization caused by condensation and cloud nucleation is nearly everywhere higher than stabilization caused by dry dynamics, and is the primary process through which high static stability is found along the frontal surface. The frontogenesis and static stability tendency equations are combined to form an expression for the frontal slope tendency. While dynamic processes lead to increases in frontal slope, latent heating often counteracts this tendency. This indicates that the direct effect of latent heating on the thermal structure of the front is to decrease the slope and in that sense weaken the warm front.

Key Words: warm fronts; cloud microphysics; diabatic effects

Received 9 July 2012; Revised 8 January 2013; Accepted 10 January 2013; Published online in Wiley Online Library 15 March 2013

Citation: Igel AL, van den Heever SC. 2014. The role of latent heating in warm frontogenesis. *Q. J. R. Meteorol. Soc.* **140**: 139–150. DOI:10.1002/qj.2118

1. Introduction

The role of latent heating in frontogenesis – the process through which horizontal temperature gradients are strengthened – has been extensively studied, especially through modelling experiments (Baldwin *et al.*, 1984; Hsie *et al.*, 1984; Thorpe and Emanuel, 1985; Chan and Cho, 1991; Montgomery and Farrell, 1991; Posselt and Martin, 2004). Through these efforts it is known that latent heating strongly influences frontal speed and is important for the mesoscale structure of vertical velocity, rain bands and the formation of the occlusion in extratropical cyclones. Multiple studies have shown that vertical velocities are increased, updraughts are narrowed and the horizontal ageostrophic circulation is increased when the effects of latent heating are included in numerical models (Baldwin *et al.*, 1984; Thorpe and Emanuel, 1985; Han *et al.*, 2007). The contributions of latent heating to frontogenesis at mid levels seem to be particularly important for the formation of

rain bands (Novak *et al.*, 2009; Baxter *et al.*, 2011). However, the mechanisms through which the impacts discussed above are realized are not well understood. For example, it is unclear if frontal speed is increased due to increases in the cross-frontal circulation in the presence of latent heating or whether it is increased due to the creation and propagation of potential vorticity (PV) anomalies that act to alter the wind fields (Reeves and Lackmann, 2004).

Furthermore, aside from condensation, which is the focus of most of the studies reported in the literature, there has been little examination of the relative importance of individual microphysical processes in latent heating and frontogenesis. Evaporation and sublimation have been found to enhance downdraughts (Huang and Emanuel, 1991; Parker and Thorpe, 1995; Clough *et al.*, 2000) and melting may accelerate surface frontogenesis in winter storms (Szeto and Stewart, 1997). All but one of these studies employed an idealized one- or two-dimensional model framework and all use relatively simple microphysics

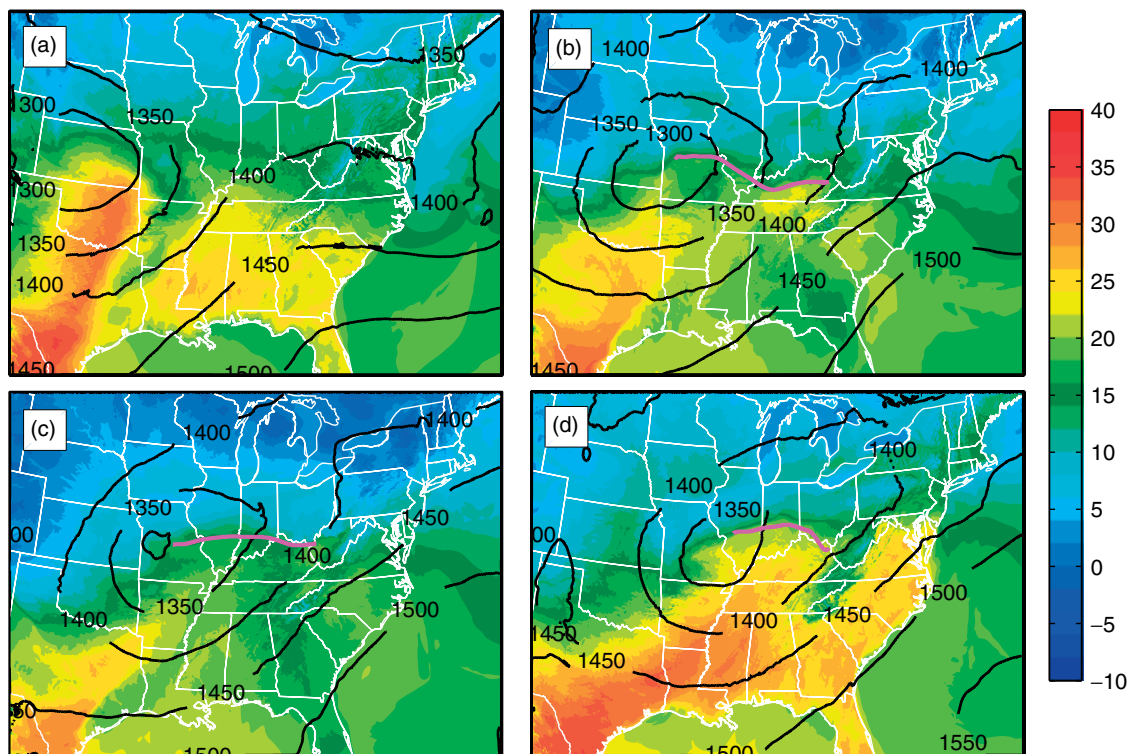


Figure 1. RAMS output from the inner grid of surface temperature ($^{\circ}\text{C}$, shaded), 850 mb geopotential height (contoured), and the objectively analysed warm front location (heavy pink) at (a) 1800 UTC (1200 CST) 9 April, (b) 0600 UTC (0000 CST) 10 April, (c) 1200 UTC (0600 CST) 10 April, and (d) 1800 UTC (1200 CST) 10 April 2009. Modified after Igel *et al.* (2013).

parametrizations. A better understanding of the role of individual microphysical processes could help to explain the spectrum of responses to latent heating that have been observed in fronts.

The focus of this study will be on the direct role of latent heating, both total latent heating and latent heating from individual cloud processes, on the warm front. Joos and Wernli (2011) examined the role of depositional growth of snow, cloud condensation/evaporation, melting of snow and evaporation of rain in the modification of potential vorticity along the warm conveyor belt through the use of trajectory analysis and in doing so presented a budget of latent heating. In the present study we will extend that work by developing a budget for latent heating in the warm front region that considers the contribution from cloud nucleation separate from cloud condensation in addition to the contributions from processes presented by Joos and Wernli (2011). Additionally, the role of each latent heat process to the frontogenesis and static stability tendency equations will be assessed. Furthermore, these equations will be combined to examine the rate of change of the frontal slope in order to evaluate the overall impact of latent heating on the thermal structure of the front.

2. Methods

2.1. Model set-up and storm evolution

In this study we examine the warm front of an extratropical cyclone that crossed the USA from 9 to 11 April 2009. The Regional Atmospheric Modeling System (RAMS) (Pielke, *et al.*, 1992; Cotton *et al.*, 2003) was used to simulate the storm (Igel *et al.*, 2013). The set-up consisted of two nested grids, with the outer grid covering the majority of the USA at

15 km horizontal grid spacing and the inner grid extending from the Rockies to the coast of Maine at 3 km horizontal grid spacing. The location of the inner grid is depicted in Figure 1. Both grids contained 45 vertical levels with 75 m spacing at the surface expanding to 1 km spacing near the model top. A two-moment bin-emulating bulk microphysical scheme (Saleeby and Cotton, 2004, 2007) that prognoses the mixing ratio and number concentration of five ice species (pristine ice, snow, aggregates, graupel and hail) and three liquid species (two cloud droplet modes and rain) and that also tracks the rates of many microphysical processes (deposition, condensation, melting, etc.) was used.

The model was initialized at 0000 UTC 9 April 2009 using the corresponding Global Forecast System (GFS) analysis file and integrated for 48 h, with subsequent GFS analysis files being used to nudge the lateral boundaries. Figure 1 shows surface analyses of various storm characteristics over the course of the simulation. It possessed an elongated, well-defined warm front that persisted for about 16 h and caused widespread precipitation from Missouri to Ohio. A warm front, located south of the storm centre, was associated with a severe weather outbreak in the southeast USA. The model reproduced the observed warm frontal structure and accumulated precipitation well (Igel *et al.*, 2013).

2.2. Objective front detection

An objective front detection algorithm based on the method of Hewson (1998) was applied to the output to locate the warm front. A full description of the frontal detection used in this analysis is given in Igel *et al.* (2013). Briefly, fronts are identified where the along-vector gradient of $\nabla|\nabla\theta|$ at the surface is zero, where θ is potential temperature, and then the geostrophic wind (V_g) is used to separate warm from cold

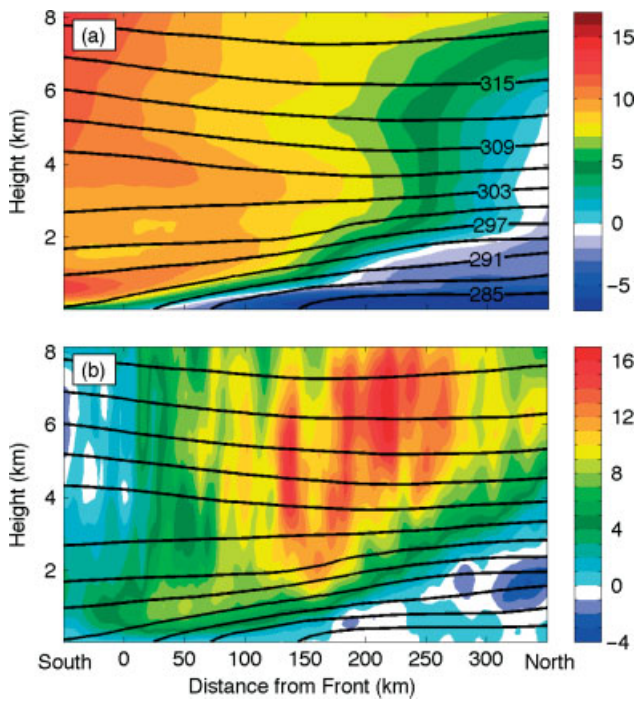


Figure 2. Composite cross-sections of (a) cross-front wind velocity (m s^{-1}) and (b) vertical velocity (cm s^{-1}). The black lines are isentropes (K).

fronts. Additional objective masks were applied to remove fronts that were located along land–water boundaries, the warm front associated with the severe weather outbreak and fronts that were not continuous in time. The algorithm was run for every output hour. Three of the objectively identified fronts are shown in Figure 1, in which it can be seen that the fronts lie approximately in the zonal direction. All fronts were defined to have the same length and begin at a constant distance from the low-pressure centre. In this way, each front analysis contained the same number of points.

Fields output by the model were smoothed by replacing each data point with the average of the points in a 7×7 box centred on itself; then any fields derived from this smoothed output (such as frontogenesis and stability tendency terms) were calculated. All fields were subsetting relative to the front and averaged over hours 27–42 of the simulation, during which the warm front was well defined, and in the along-front direction to obtain zonally averaged cross-sections perpendicular to the front.

Figure 2 shows the average front-normal cross-sections of potential temperature and meridional and vertical winds. As expected, the surface position of the front is located on the warm side of the baroclinic zone and air is rising up and over the front. There is convergence present across the frontal zone in the meridional wind field and the maximum winds are found 0.5–1 km above the surface. Figure 3 shows average cross-sections of the horizontal and vertical gradients of potential temperature. These figures further confirm that the frontal detection algorithm has been successful. Furthermore, the ridge of maximum values extending from the surface in these fields indicates the position of the frontal surface and will aid the discussion below. Further details on the evolution of the simulated storm and the objective frontal detection algorithm are described in Igel *et al.* (2013).

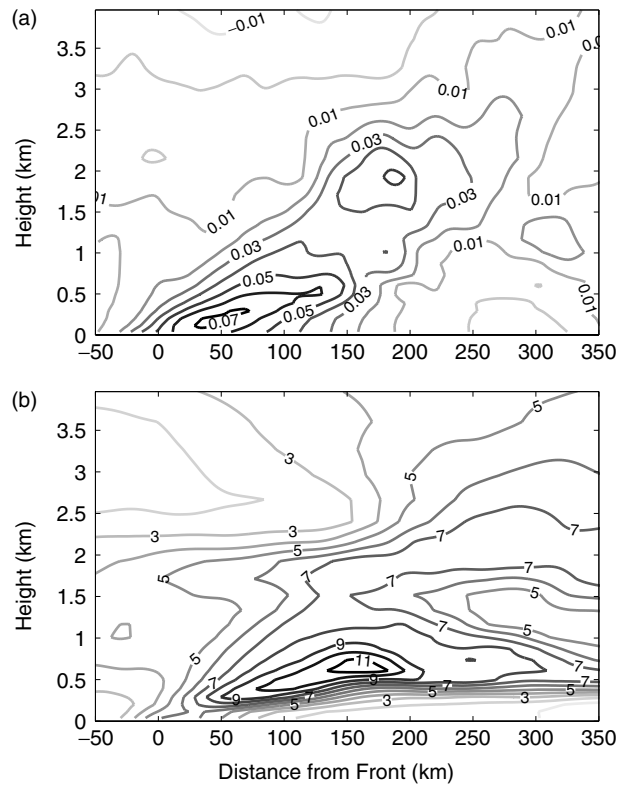


Figure 3. (a) Negative of the horizontal gradient and (b) vertical gradient of potential temperature in K km^{-1} . Note that the vertical axis is different from that in Figure 2.

2.3. Frontogenesis and static stability tendency equations

Both the frontogenesis and static stability tendency equations will be examined. The meridional front-normal component of frontogenesis is expressed as

$$\frac{d}{dt} \left(-\frac{d\theta}{dy} \right) = \underbrace{\frac{\partial u}{\partial y} \frac{\partial \theta}{\partial x}}_a + \underbrace{\frac{\partial v}{\partial y} \frac{\partial \theta}{\partial y}}_b + \underbrace{\frac{\partial w}{\partial y} \frac{\partial \theta}{\partial z}}_c - \underbrace{\frac{\theta}{T c_p} \frac{\partial}{\partial y} \left(\frac{dQ}{dt} \right)}_d \quad (1)$$

and is similar to the form used by Keyser and Pecnick (1985). The coordinate axes are defined such that the x -axis is in the zonal direction and approximately parallel to the front (see Figure 1), the y -axis points to the north and z is defined as the height above the surface. In the above equation u is the zonal wind velocity, v is the meridional wind velocity, w is the vertical velocity, T is the temperature, c_p is the specific heat of air at constant pressure, and dQ/dt is the diabatic heating rate. There are four terms on the right-hand side (RHS) of Eq. 1: shearing deformation (a), confluent deformation (b), tilting (c) and diabatic contributions (d). Previous work has found that shearing deformation is much smaller than confluent deformation in the region of warm fronts due to small zonal gradients in potential temperature (Han *et al.*, 2007). The same result is seen in this analysis (not shown) and hence any term containing the zonal gradient of potential temperature here and in the equations to follow will be neglected in the analysis. In addition, no equation for the evolution of $d\theta/dx$ is needed since it is assumed to be small. The last term, the diabatic contribution, takes into account processes such as latent heating, radiation and friction; however, this study will only consider the

contributions of latent heating processes to the diabatic term.

Frontal surfaces are known to be areas of high static stability, yet few studies have examined the evolution of the frontal structure in the vertical direction or the effect of environmental static stability on fronts, Keyser and Anthes (1982) being one of the exceptions. Most of the attention has rather been given to the evolution of horizontal potential temperature gradients, the quantity most often used to identify fronts. However, Bannon (1984) found that fronts evolving in environments with relatively high static stability move more slowly, possess weaker horizontal potential temperature gradients and are less steeply sloped than fronts evolving in environments with lower static stability, due to suppressed vertical motions. While the stability of the environment and the stability of the frontal zone are not the same, the results of Bannon (1984) indicate that the vertical structure of frontal zones can be important for the evolution of the front as a whole and should not be so routinely disregarded in frontal studies.

The vertical component of the frontogenesis equation can be used to understand the formation of zones of high static stability and inversions that are associated with fronts (Miller, 1948). Similarly to the equation for the horizontal component (Eq. (1)), it can be expressed as

$$\frac{d}{dt} \left(-\frac{d\theta}{dz} \right) = -\frac{\partial u}{\partial z} \frac{\partial \theta}{\partial x} - \overbrace{\frac{\partial v}{\partial z} \frac{\partial \theta}{\partial y} - \frac{\partial w}{\partial z} \frac{\partial \theta}{\partial z}}^e + \overbrace{\frac{\theta}{Tc_p} \frac{\partial}{\partial z} \left(\frac{dQ}{dt} \right)}^f. \quad (2)$$

The first two terms on the RHS describe the tilting of isentropes and the third term captures the stretching of isentropes. Again, as with Eq. (1), the first term on the RHS will be neglected. However, expansion of the first two terms into their geostrophic and ageostrophic contributions would show that the geostrophic contributions cancel. Nonetheless, we have used the full winds in the calculation of term e since we have found the geostrophic contribution in the vicinity of the front to be small (not shown). Term e in Eq. (2) will be called the ‘dynamic term’ and term f the ‘diabatic term’. Considering only the dynamic terms of Eqs (1) and (2), one can see that the only difference is that the partial derivatives involving wind speeds are taken with respect to different coordinates. A typical value for $\partial v/\partial y$ in the vicinity of a frontal surface is $\sim 10 \text{ m s}^{-1} (100 \text{ km})^{-1}$, whereas $\partial v/\partial z$ is about $100\times$ greater at $\sim 10 \text{ m s}^{-1} \text{ km}^{-1}$. A similar relationship exists between the meridional and vertical derivatives of w . Therefore, the static stability tendency should be at least ~ 2 orders of magnitude greater than horizontal frontogenesis.

Fronts have two primary effects on local weather: they bring sudden changes in temperature, and they often are associated with cloud cover and precipitation. The horizontal potential temperature gradient (or other density gradient proxy) is the traditional metric used to characterize the strength of a front and measures the first impact of fronts very well; however, it may also be desirable to characterize the strength of a front by its ability to produce clouds and precipitation. While water vapour availability is of course important to cloud formation, vertical velocity is crucial

to this process. In practice, vertical velocity is difficult to measure, but an estimate of the forcing of vertical velocity can be made through use of the quasi-geostrophic omega equation. Therefore we propose that the forcing of vertical motion be considered as an alternative definition of frontal strength.

To investigate the forcing of vertical motion at frontal boundaries, the Q-vector form of the quasi-geostrophic omega equation is given in its expanded form by

$$\left(\sigma \nabla^2 + \nabla^2 \sigma + f_o^2 \frac{\partial^2}{\partial p^2} \right) \omega = -2 \nabla \cdot \mathbf{Q} \\ = -2f\gamma \left\{ \overbrace{\left[\frac{\partial}{\partial x} \left(-\frac{\partial \mathbf{V}_g}{\partial x} \right) \cdot \nabla \theta + \frac{\partial}{\partial y} \left(-\frac{\partial \mathbf{V}_g}{\partial y} \right) \cdot \nabla \theta \right]}^A \right. \\ \left. + \overbrace{\left[-\frac{\partial \mathbf{V}_g}{\partial x} \cdot \nabla \left(\frac{\partial \theta}{\partial x} \right) - \frac{\partial \mathbf{V}_g}{\partial y} \cdot \nabla \left(\frac{\partial \theta}{\partial y} \right) \right]}^B \right\} \quad (3)$$

(Martin, 1998), where we have relaxed the assumption of a base state stability, $\sigma \equiv -RT(p\theta)^{-1} \partial \theta / \partial p$, $\gamma = (R/fp_o)(p_o/p)^{c_p}$, f is the Coriolis parameter, p is pressure and ω is the pressure velocity. Scale analysis shows that $\sigma \sim 10^{-6}$, $f_o^2 \sim 10^{-8}$ and $\partial^2/\partial p^2 \sim 10^{-10}$. In the front-normal direction the length scale L is $\sim 100 \text{ km}$, and in the along-front direction $L \sim 1000 \text{ km}$, corresponding to $\nabla^2 \sim 10^{-11}$. Therefore, the third operator on the LHS of Eq. (3) is an order of magnitude less than the first two operators and can be neglected. It would appear that the remaining two operators are of the same magnitude. However calculation of these terms in the area of the warm front in this simulation showed that the second operator is in fact an order of magnitude larger than the first (Figure 4). Therefore, the first operator can also be neglected. With these results, the static stability parameter can be brought over to the RHS of Eq. (3), yielding

$$\nabla^2 \omega \approx -2f\gamma \\ \left\{ \overbrace{\left[\frac{\partial}{\partial x} \left(-\frac{\partial \mathbf{V}_g}{\partial x} \right) \cdot \frac{\nabla \theta}{\sigma} + \frac{\partial}{\partial y} \left(-\frac{\partial \mathbf{V}_g}{\partial y} \right) \cdot \frac{\nabla \theta}{\sigma} \right]}^A \right. \\ \left. + \frac{1}{\sigma} \overbrace{\left[-\frac{\partial \mathbf{V}_g}{\partial x} \cdot \nabla \left(\frac{\partial \theta}{\partial x} \right) - \frac{\partial \mathbf{V}_g}{\partial y} \cdot \nabla \left(\frac{\partial \theta}{\partial y} \right) \right]}^B \right\}, \quad (4)$$

where $\nabla \theta/\sigma$ is essentially the slope of the isentropes. According to Eq. (4), the slope of a front will be proportional to the forcing for vertical motion through term A . If, as we have suggested, the frontal intensity or strength is defined to describe the forcing of vertical velocity at a front, then the isentropic slope rather than the horizontal potential temperature gradient is a simple metric that may be more appropriate for characterizing frontal strength. By this definition, a decreased slope should lead to decreases in vertical velocities and in that sense should weaken a front, even if horizontal frontogenesis occurs, as shown in the schematic in Figure 5.

There are limitations to quasigeostrophic theory in frontal zones. In particular, it does not account for action by the

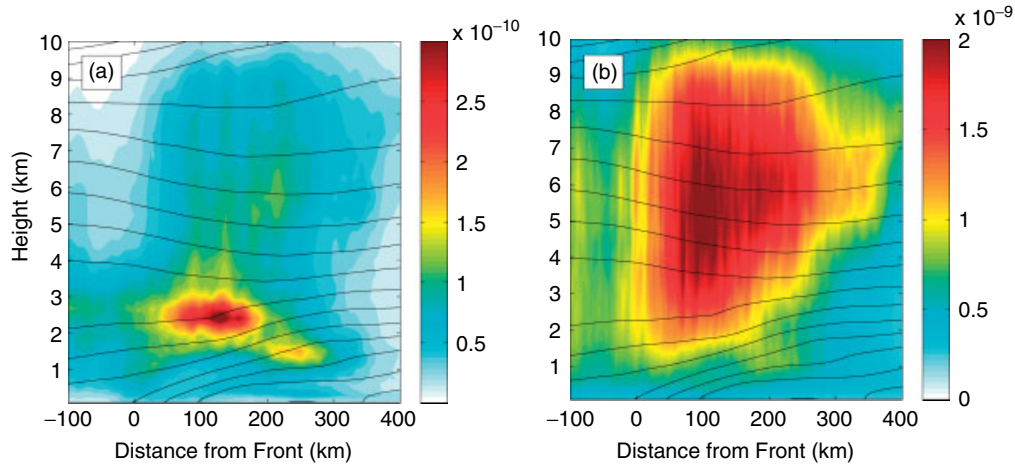


Figure 4. Composite cross-sections of the absolute value of (a) $w(\partial\theta/\partial z)^{-1}\nabla^2(\partial\theta/\partial z)$ and (b) ∇^2w in units of $\text{K m}^{-2} \text{s}^{-1}$. These terms correspond to the first and second operators of Eq. (3) divided by σ but in Cartesian coordinates and with common factors neglected. Thin black lines are isentropes.

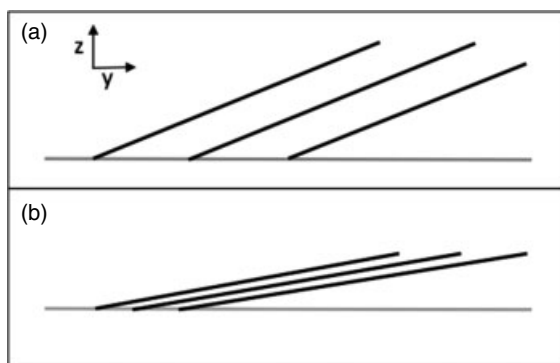


Figure 5. A simple schematic of a warm front where the black lines represent isentropes. In (b), both the horizontal and vertical gradients of potential temperature have increased over their values in (a), but the slope has decreased and so in that sense the front has weakened. See text for further discussion.

ageostrophic wind, latent heating or frictional effects, all of which can be large. In addition, the isentropic slope does not appear in term B in Eq. (4). Nonetheless, we do feel that slope may be a better indicator of frontal strength than $\nabla\theta$ because of its relationship with vertical motion, as discussed above. We do not necessarily feel that slope should be used to identify fronts, only to characterize their intensity. One point to make is that slope and horizontal temperature gradient will not always agree on the relative strength of fronts, as shown in Figure 5, but, once again, using slope to characterize fronts may still lend insight into their dynamics.

An equation can be constructed that expresses the rate of change of the slope of the isentropes. First, the chain rule can be used to express the slope of the isentropes as the negative ratio of the horizontal θ gradient to the vertical θ gradient as follows:

$$d\theta(y, z) = \frac{d\theta}{dy}dy + \frac{d\theta}{dz}dz = 0, \quad (5)$$

$$\left. \frac{dz}{dy} \right|_{\theta} = \frac{-\frac{d\theta}{dy}}{\frac{d\theta}{dz}}. \quad (6)$$

Next, the total time derivative is taken on both sides of Eq. (6). One can invoke the chain rule again to express the

time rate of change of the slope as

$$\frac{d}{dt} \left(\left. \frac{dz}{dy} \right|_{\theta} \right) = \frac{\frac{d\theta}{dz} \frac{d}{dt} \left(-\frac{d\theta}{dy} \right) + \frac{d\theta}{dy} \frac{d}{dt} \left(\frac{d\theta}{dz} \right)}{\left(\frac{d\theta}{dz} \right)^2}, \quad (7)$$

as was previously done by Van Delden (1999). The LHS of Eq. (7) is defined here as the *slope tendency* of the front. It is a function of the meridional and vertical θ gradients, and the frontogenesis and static stability tendency equations. A similar equation could be constructed for the slope in the zonal direction as well. As shown previously, horizontal frontogenesis is $\sim 100\times$ smaller than the static stability tendency; however, $d\theta/dz$ is $\sim 100\times$ greater than $d\theta/dy$ along the frontal surface (Figure 3). Therefore, the terms in the numerator of Eq. (7) should be of equal magnitude and compete for dominance.

The expressions for the two components of frontogenesis (Eqs (1) and (2)) can be substituted into Eq. (7). After reordering the terms, the slope tendency can be written as

$$\frac{d}{dt} \left(\left. \frac{dz}{dy} \right|_{\theta} \right) = \frac{\overbrace{\left(\frac{d\theta}{dz} \left(\frac{\partial v}{\partial y} \frac{\partial \theta}{\partial y} + \frac{\partial w}{\partial y} \frac{\partial \theta}{\partial z} \right) \right)}^g + \frac{d\theta}{dy} \left(-\frac{\partial v}{\partial z} \frac{\partial \theta}{\partial y} - \frac{\partial w}{\partial z} \frac{\partial \theta}{\partial z} \right)}{\underbrace{\left(-\frac{\theta}{Tc_p} \left\{ \frac{d\theta}{dz} \frac{\partial}{\partial y} \left(\frac{dQ}{dt} \right) + \frac{d\theta}{dy} \frac{\partial}{\partial z} \left(\frac{dQ}{dt} \right) \right\} \right)}_h} \left(\frac{d\theta}{dz} \right)^2}. \quad (8)$$

The terms with zonal gradients of potential temperature have been dropped since it was assumed previously that they are negligible. Term g in Eq. (8) is the dynamic contribution to the slope tendency and term h the diabatic contribution. The units of the slope tendency will be expressed as $\text{m km}^{-1} \text{h}^{-1}$ and can be interpreted as the rise or fall (in metres) of an isentrope per kilometre in the horizontal per hour. A typical slope of the warm front in this simulation is $\sim 10 \text{ m km}^{-1}$. This is in agreement with the observations of Kemppi and Sinclair (2011), who found warm frontal slopes ranging from 6 to 18 m km^{-1} .

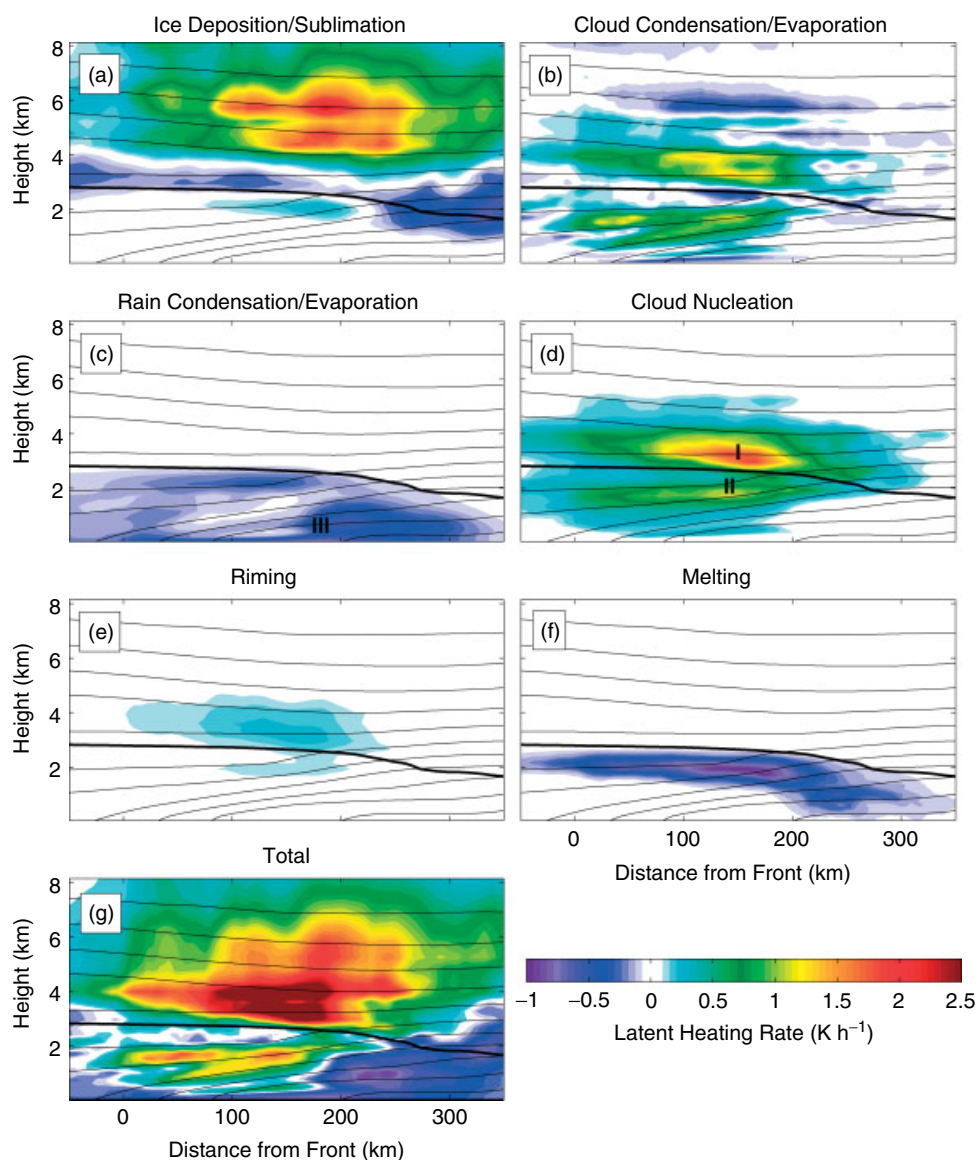


Figure 6. Temporally and zonally averaged cross-sections of the latent heating rate (K h^{-1}) of (a–f) the six most important microphysical processes acting along the warm front and (g) their total. The thin black lines are isentropes and the thick black line is the 0° isotherm.

3. Results

3.1. Latent heating budget

Figure 6 shows the zonally and temporally averaged spatial distribution of the six primary microphysical processes that contribute to latent heating within the warm frontal cloud, namely vapour deposition/sublimation of all ice species, condensation/evaporation of cloud droplets and rain, cloud droplet nucleation, riming of cloud droplets and rain by ice species, and melting. The RAMS microphysics scheme includes explicit activation of aerosol particles (Saleeby and Cotton, 2004). Vapour used to activate aerosol particles to cloud droplets is called cloud nucleation, whereas vapour transferred to (from) existing cloud droplets is called cloud condensation (evaporation). Vapour used to activate aerosol particles to ice crystals is also tracked separately by the model, but the contribution by that process to latent heating is at least an order of magnitude lower than the contribution by any other process (not shown). Clearly vapour deposition (Figure 6(a)) onto ice is the largest contributor to latent

heating, both in the absolute maximum at any point and in total when integrated over the domain. However, since latent heat release associated with this process is mostly confined to 4 km and above, it has little direct influence on the frontal zone itself. To be clear, latent heating due to vapour deposition can lead to the creation or destruction of upper-level potential vorticity, which can then influence lower levels and the front itself, but the heating does not have a direct impact on the isentropic structure of the warm frontal surface.

Latent heating from vapour condensation (Figure 6(b)) and cloud nucleation (Figure 6(d)) rival that of vapour deposition in magnitude, but are much closer spatially to the frontal surface and can therefore have a larger influence. Two maxima exist in the cloud condensation and cloud nucleation fields, labelled I and II in Figure 6(d). The upper peak is due to supersaturated conditions associated with peaks in updraught velocities, while the lower peak is associated with the melting layer (Figure 6(f)), where the latent cooling by melting is helping to create supersaturated conditions (Woods *et al.*, 2008). Although the heat absorbed

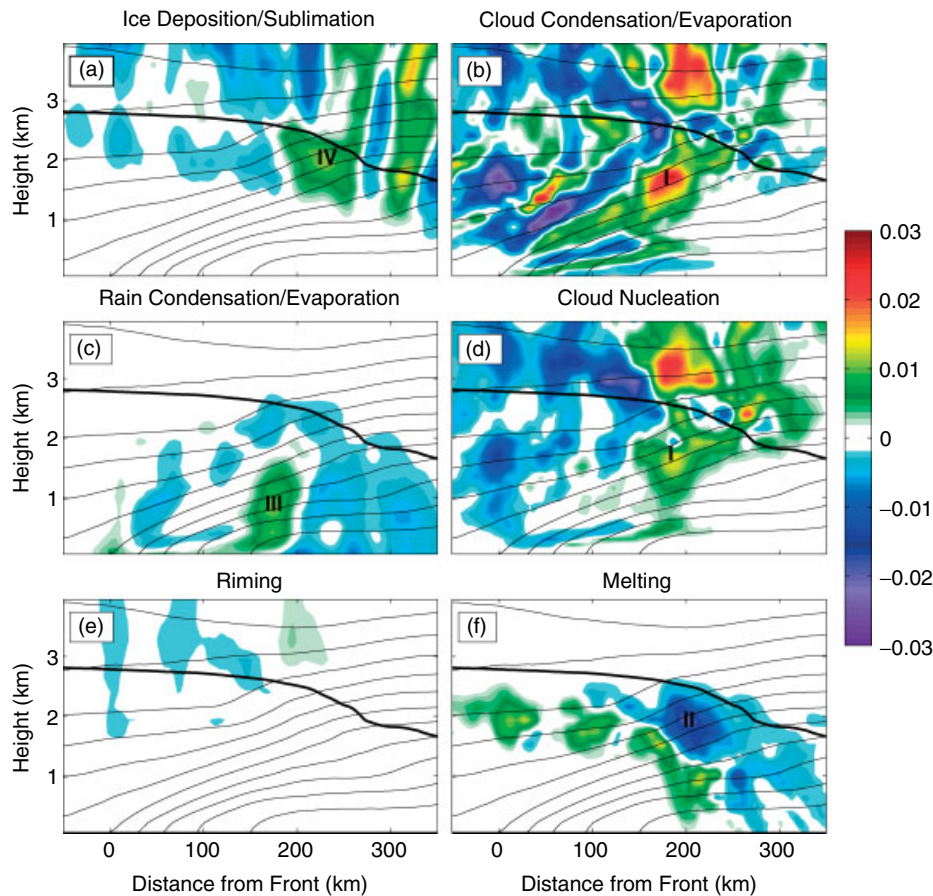


Figure 7. Temporally and zonally averaged cross sections of horizontal frontogenesis ($\text{K km}^{-1} \text{h}^{-1}$) of the six most important microphysical processes acting along the warm front. Note that the upper limit on the vertical axis is reduced from that used in Figure 6. The thin black lines are isentropes and the thick black line is the 0° isotherm.

per kilogram of melting ice is an order of magnitude less than that associated with evaporation or sublimation, the maximum latent cooling from melting has a similar magnitude to the maxima of vapour to ice, vapour to cloud and cloud nucleation. This is because ice must melt in a shallow layer due to a sufficiently rapid increase in temperature below the melting level (Clough *et al.*, 2000); therefore, the rate of melting is about an order of magnitude greater than that of any other microphysical process. However, since the melting is collocated with condensation and nucleation, there is little net latent heating or cooling directly beneath the melting level (Figure 6(g)).

Evaporation of rain (Figure 6(c)) is widespread beneath the melting level and maximizes around 200 km ahead of the front at location III due to low relative humidity in the dry continental air mass and because the rain is heaviest there due to a maximum in the vertically integrated melting rate. Overall, the relative contributions of condensation, deposition and evaporation of rain are in agreement with the findings of Joos and Wernli (2011), who examined the latent heating budget of parcel trajectories along the warm conveyor belt. In their study latent cooling due to melting was much less, but this would be expected for parcels with predominantly rising trajectories upwind of the front that do not pass through the area of strongest melting.

Finally, riming contributes very little to the total latent heating. Like melting rates, riming rates would need to be an order of magnitude larger than those of liquid-vapour or ice-vapour processes in order to achieve high latent heating

rates. However, since riming is not confined to occur in a shallow layer as melting is, these high rates are not achieved.

3.2. Frontogenesis

We will now examine the rates of horizontal frontogenesis associated with each of the microphysical processes (Eq. (1), term d ; Figure 7) and how they compare to the rates from the dynamic terms (Eq. (1), terms b, c ; Figure 8). Horizontal frontogenesis due to latent heating will occur where there is a negative gradient of latent heating in the cross-front direction. Of all the processes, horizontal frontogenesis due to cloud condensation (Figure 7(b)) is largest, particularly along the frontal surface from 25 to 200 km ahead of the front (location I in Figure 7(b)). Cloud nucleation (Figure 7(d)) also produces significant values, but not until $\sim 150\text{--}200$ km ahead of the front at location I, where they serve to reinforce the pattern found in cloud condensation. These locations for frontogenesis arise since the maximum in latent heating for these two processes occurs along and just above the frontal surface (Figure 6(b), (d)) since air must rise over this surface. As a result, we would expect frontogenesis due to these processes to occur along the frontal surface of most fronts if supersaturation is present. Melting shows some high frontolysis rates at location II (Figure 7(f)), where the melting level begins to slope downward and melting itself is beginning to decrease. However, the frontolysis rates are largely negated by the frontogenesis due to the cloud liquid processes (Figure 7(b), (c)). Evaporation of rain

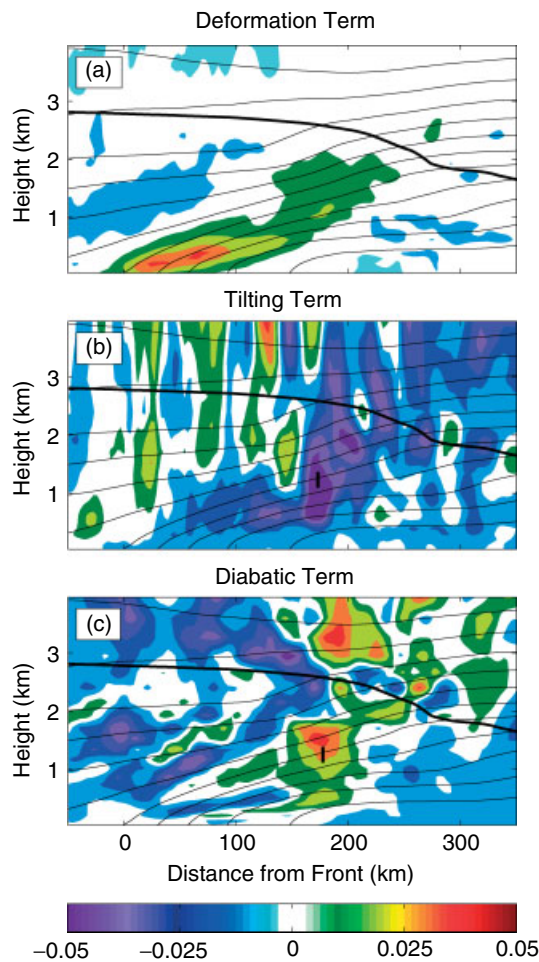


Figure 8. Temporally and zonally averaged cross-sections of the (a) deformation, (b) tilting, and (c) diabatic terms of the horizontal frontogenesis equation ($\text{K km}^{-1} \text{h}^{-1}$). The thin black lines are isentropes and the thick black line is the 0° isotherm.

(Figure 7(c)) plays a modest role and also serves to strengthen the frontogenesis associated with cloud condensation at location III. This location would be expected to vary with the location of maximum evaporation. Vapour deposition onto ice (Figure 7(a)) does contribute somewhat to frontogenesis at mid levels far ahead of the front (location IV) and further counteracts the frontolysis due to melting. As expected from the previous section, riming is negligible.

The deformation, tilting and total diabatic terms are shown in Figure 8. The deformation term (Figure 8(a)) is the most spatially uniform of the three and contributes most to frontogenesis at and just above the surface. The tilting term (Figure 8(b)) is mostly frontolytic and the maxima in the tilting and diabatic terms, located 150–200 km ahead of the front at location I in Figure 8, oppose one another. This pattern agrees with the results of previous studies (Han *et al.*, 2007, and references therein) that showed that the tilting and deformation terms should generally oppose one another in sign. As seen in Figure 8(c), the primary impact of the diabatic term is to increase frontogenesis between ~ 0.5 and 2 km above the surface, but ~ 175 km from the surface location of the front. This is consistent with Hsie *et al.* (1984), who found the largest increases in the horizontal temperature gradient at mid levels when condensation and evaporation were included in an idealized simulation of a cold front.

Figure 9 shows how the frontogenesis terms vary in the along-front direction and in time. All frontogenesis terms, especially the deformation term, weaken with increasing distance from the storm centre. Tilting is the most variable in sign; however, in general the patterns of frontogenesis and frontolysis are consistent in space in time, as are the relative magnitudes of the terms. Based on Figure 9, the mean appears to represent the processes at the warm front well both spatially and temporally. Similar analyses have been done for the other processes presented as a mean in this study and have comparable results, but are not shown.

3.3. Static stability tendency

When considering microphysical processes, one would expect large gradients both in the vertical direction as well in the horizontal direction. Indeed, this is the case, as seen in Figure 10, which shows the static stability tendency due to individual microphysical processes. Distinct layers of stabilization and destabilization exist in all fields except riming. Vapour deposition (Figure 10(a)) is still too far removed from the frontal surface to play much of a role, and the effects of melting (Figure 10(f)) and cloud liquid processes (Figure 10(b), (d)) again oppose each other to some extent just below the freezing level. Some of the highest rates of stabilization occur just above the surface in association with the cloud boundary (location I in Figure 10(b)), where there is a sharp transition from condensation to evaporation (Figure 6(b)). Just below this, evaporation of rain (Figure 10(c)) also has a very strong signal that is confined to a shallow layer near the surface. Although the absolute magnitude of rain evaporation is not large, rain evaporation does have a large vertical gradient and it makes a significant contribution to the static stability tendency. Finally, the sum of these terms, the total diabatic term (Figure 11(b)), is almost everywhere larger than the dynamic term (Figure 11(a)) and dominates the total static stability tendency (Figure 11(c)).

The dynamic stability tendency term is positive along the frontal surface out to ~ 150 km, at which point it becomes negative (location I, Figure 11(a)) because vertical gradients in w (Figure 2(b)) begin to dominate the dynamic term. At the surface, ahead of the front at location II, the dynamic term is also destabilizing. This latter shift occurs because the strongest meridional winds occur just above the surface (Figure 2(a)), leading to a reversal in wind shear that changes the sign of the first term in e in Eq. (2).

3.4. Slope tendency

Figure 12 shows the dynamic, diabatic and total slope tendencies of the front. Even though the potential temperature field is smoothed as described in section 2.2, static stability is near zero at some grid points such that the calculation of slope tendency yields unrealistically large numbers due to division by the square of static stability in Eq. (7). Therefore all rates greater than $100 \text{ m km}^{-1} \text{h}^{-1}$ have been removed. This is a subjective threshold, but the pattern of slope tendency was seen to be insensitive to the choice of threshold value.

There is strong dynamic positive slope tendency at the surface (location I, Figure 12(a)) associated with the elevation of the strongest low-level winds (Figure 2(a)).

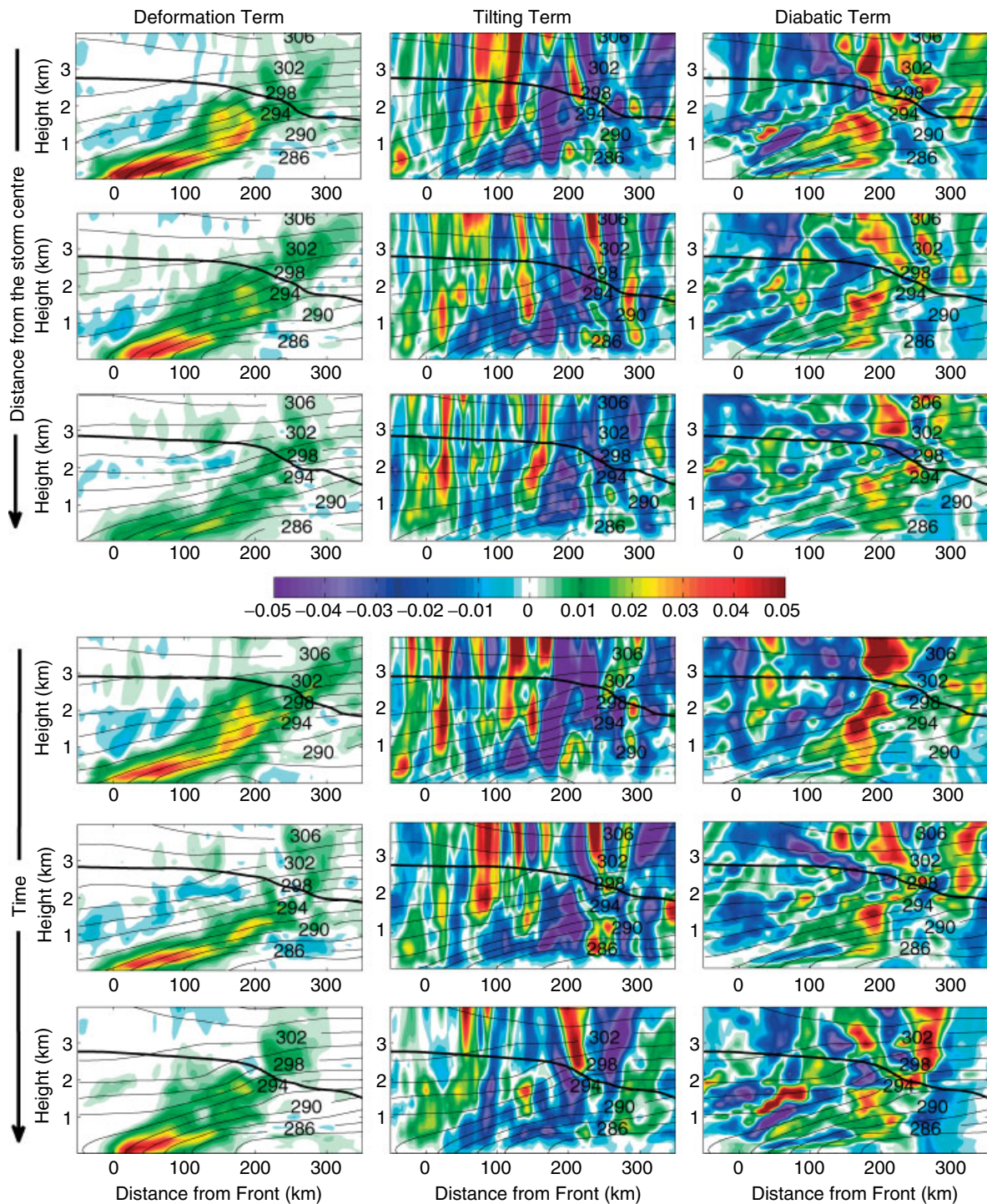


Figure 9. Composite cross-sections of the deformation, tilting and diabatic terms of the frontogenesis equation. The first three rows are averaged over hours 27–42 of the simulation and each row is averaged over a third of the data in the along-front direction, where the first row shows the third closest to the storm centre, the second row shows data from the middle third and the third row shows data from the third farthest from the storm centre. The second three rows are averaged over the full along-front distance and each row is averaged over a third of the time period, where the fourth row is averaged over hours 27–31, the fifth row over hours 32–36 and the sixth row over hours 37–42. The thin black lines are isentropes and the thick black line is the 0° isotherm.

Elsewhere along the frontal surface positive and negative values can be found; this pattern reflects the competing nature of the confluent and tilting terms of the horizontal frontogenesis. There is significant flattening of the isentropes below the melting level at and beyond 175 km from the surface front that is primarily caused by frontolytic tilting in the horizontal (Figure 8(b)). In this region the dynamic slope tendency dominates the total slope tendency seen in Figure 11(c).

The diabatic slope tendency is generally small around the melting level and along the frontal surface, despite relatively large values of destabilization and stabilization at those locations, respectively. This is because the diabatic horizontal frontogenesis and stability tendency terms often have the same sign in these regions, thus leading to cancellation of the two slope tendency terms in h in Eq. (8) (the horizontal and vertical gradients of potential temperature have opposite signs nearly everywhere). At and just above

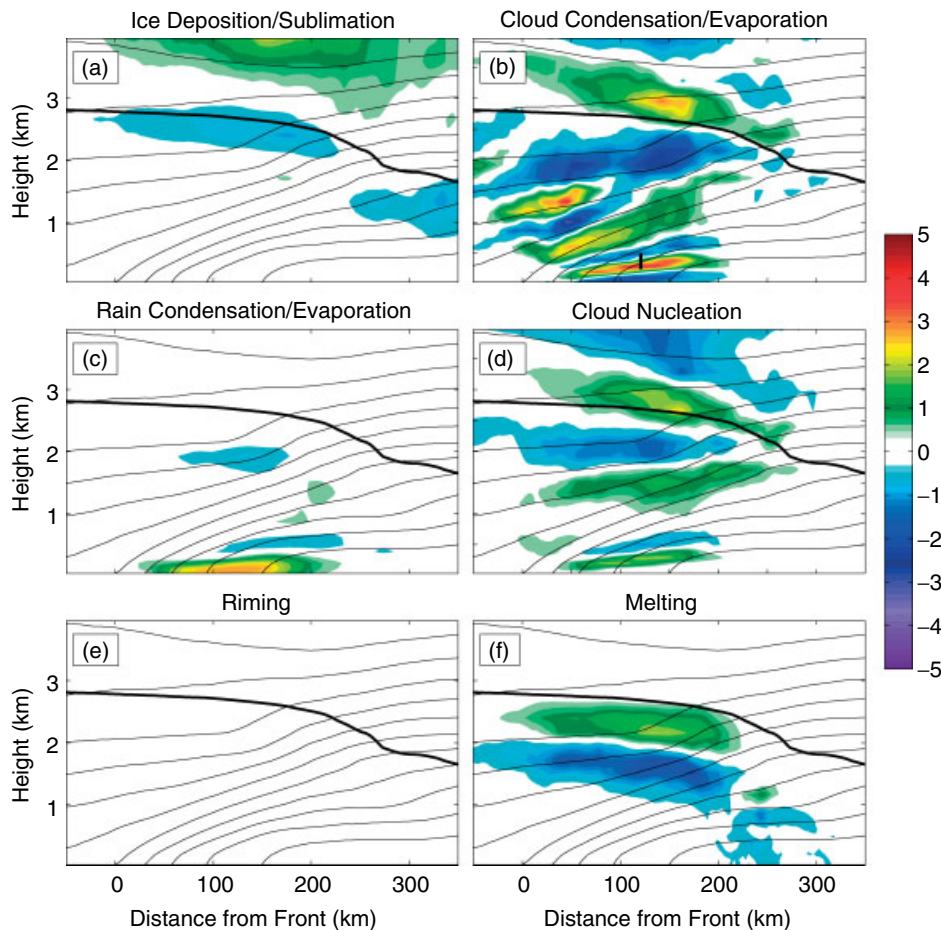


Figure 10. Temporally and zonally averaged cross-sections of the static stability tendency ($\text{K km}^{-1} \text{h}^{-1}$) of the six most important microphysical processes acting along the warm front. The thin black lines are isentropes and the thick black line is the 0° isotherm.

the surface, however, there are large negative values of slope tendency associated with the evaporation of cloud and rain (location II, Figure 12(b)) that counteracts the dynamic slope tendency. Upwind of the front (location III) the diabatic term is also negative and suppresses much of the change in slope being produced there through dynamic processes (Figure 12(c)). In fact, the diabatic slope tendency is almost everywhere negative, indicating that latent heating consistently acts to decrease the slope of the front and weaken the updraughts forced by dry dynamics according to Eq. (4). That is not to say that latent heating does not locally enhance updraughts, which it does, but rather that latent heating causes the frontal structure itself to become less favourable for the formation of updraughts through dry processes. Latent heating may also impact the wind and deformation fields, but those effects have not been accounted for here.

4. Conclusions

RAMS has been used to simulate an extratropical cyclone at high resolution. First the latent heating budget associated with the warm front was examined. We found that vapour deposition is the largest source of latent heat, but that condensation and the nucleation of cloud droplets contributed most significantly near the frontal surface. Melting provided the largest source of latent cooling, though it was approximately offset by the condensation

and nucleation of cloud droplets that it fostered. Latent heating from riming was found to be negligible. While these patterns of latent heating are likely to be seen in other warm-season warm fronts, different relationships between latent heating processes may arise in colder storms where melting does not exist or occurs at the surface and where vapour deposits onto ice at lower elevations.

Although vapour deposition onto ice was the largest source of latent heat, it was too far removed from the frontal surface to contribute significantly to frontogenesis. Instead, condensation and nucleation dominated the diabatic term of the frontogenesis equation. The diabatic term as a whole was found to be of comparable magnitude to the dynamic terms at mid levels, but did not contribute to frontogenesis at the surface. On the other hand, the diabatic static stability tendency term was almost everywhere larger than the dynamic vertical terms and was the primary mechanism through which high static stability was found along the frontal surface. We would expect these patterns of diabatic frontogenesis and stabilization to be commonly found in warm fronts.

The frontogenesis and static stability tendency equations were combined to calculate the frontal slope tendency. It has been argued through quasi-geostrophic theory that frontal slope can be used to quantify frontal strength; however, we do not think that it should necessarily be used to identify fronts. Dynamic processes were found to increase the slope near the surface. However, the latent heating processes tended to reduce the slope of the front

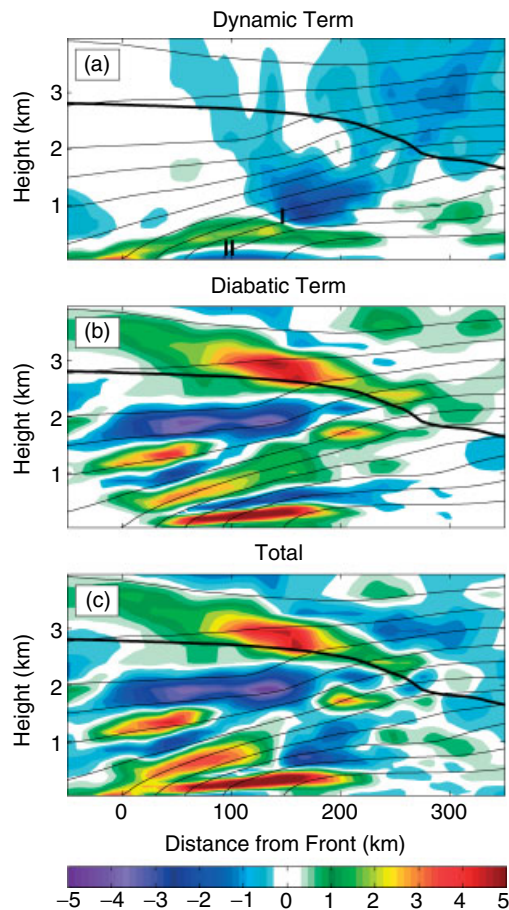


Figure 11. Temporally and zonally averaged cross-sections of the (a) dynamic and (b) diabatic terms of the static stability tendency equation and (c) their total ($\text{K km}^{-1} \text{h}^{-1}$). The thin black lines are isentropes and the thick black line is the 0° isotherm.

below 2 km, especially at the surface and upwind of the front where the dynamic slope tendency term was positive. Therefore, although latent heating did strengthen horizontal frontogenesis, the primary impact of latent heating was seen in its contribution to changes in vertical potential temperature gradients. Specifically, latent heating acted to counteract the dynamics and reduce the forcing for vertical motion at the front through a reduction in the frontal slope. This may at first seem to contradict other studies that find storm strengthening in the presence of strong latent heating (Montgomery and Farrell, 1991; Posselt and Martin, 2004; Čampa and Wernli, 2012). However, the pathways for strengthening often include the modification of potential vorticity and the dynamic fields. These previous studies address the total impact of latent heating, whereas this study only addresses the direct impact of latent heating on the isentropic structure of the warm front. Therefore, our results are not inconsistent but rather add to the complete understanding of the effects of latent heating on warm fronts.

Acknowledgements

We would like to thank Dr Jon Martin and two anonymous reviewers for their comments on the manuscript, which have led to significant improvements. This research was supported by NASA grant NNX10AM20G.

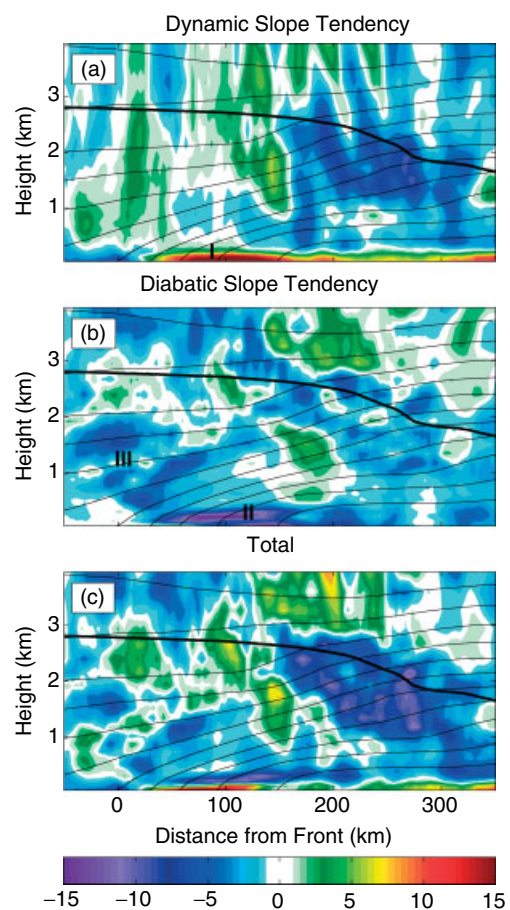


Figure 12. Temporally and zonally averaged cross-sections of the (a) dynamic and (b) diabatic terms of the slope tendency equation and (c) their total ($\text{m km}^{-1} \text{h}^{-1}$). The thin black lines are isentropes and the thick black line is the 0° isotherm.

References

- Baldwin D, Hsie E-Y, Anthes RA. 1984. Diagnostic studies of a two-dimensional simulation of frontogenesis in a moist atmosphere. *J. Atmos. Sci.* **41**: 2686–2700.
- Bannon PR. 1984. Effects of stratification on surface frontogenesis: warm and cold fronts. *J. Atmos. Sci.* **41**: 2021–2026.
- Baxter MA, Schumacher PN, Boustead JM. 2011. The use of potential vorticity inversion to evaluate the effect of precipitation on downstream mesoscale processes. *Q. J. R. Meteorol. Soc.* **137**: 179–198.
- Čampa J, Wernli H. 2012. A PV perspective on the vertical structure of mature midlatitude cyclones in the Northern Hemisphere. *J. Atmos. Sci.* **69**: 725–740.
- Chan D, Cho H-R. 1991. The dynamics of moist frontogenesis in a semi-geostrophic model. *Atmos.–Ocean*. **29**: 85–101.
- Clough SA, Lean HW, Roberts NM, Forbes RM. 2000. Dynamical effects of ice sublimation in a frontal wave. *Q. J. R. Meteorol. Soc.* **126**: 2405–2434.
- Cotton WR, Pielke RA Sr, Walko RL, Liston GE, Tremback CJ, Jiang H, McAnelly RL, Harrington JY, Nicholls ME, Carrio GG, McFadden JP. 2003. RAMS 2001: current status and future directions. *Meteorol. Atmos. Phys.* **82**: 5–29.
- Han M, Rauber RM, Ramamurthy MK, Jewett BF, Grim JA. 2007. Mesoscale dynamics of the trowal and warm-frontal regions of two continental winter cyclones. *Mon. Weather Rev.* **135**: 1647–1670.
- Hewson TD. 1998. Objective fronts. *Meteorol. Appl.* **5**: 37–65.
- Hsie E-Y, Anthes RA, Keyser D. 1984. Numerical simulation of frontogenesis in a moist atmosphere. *J. Atmos. Sci.* **41**: 2581–2594.
- Huang HC, Emanuel KA. 1991. The effects of evaporation on frontal circulations. *J. Atmos. Sci.* **48**: 619–628.
- Igel AL, van den Heever SC, Naud CM, Saleeby SM, Posselt DJ. 2013. Sensitivity of warm frontal processes to cloud-nucleating aerosol concentrations. *J. Atmos. Sci.* (in preprint, DOI:10.1175/JAS-D-12-0170.1).

- Joos H, Wernli H. 2011. Influence of microphysical processes on the potential vorticity development in a warm conveyor belt: a case-study with the limited-area model COSMO. *Q. J. R. Meteorol. Soc.* **138**: 407–418.
- Kemppi ML, Sinclair VA. 2011. Structure of a warm front: Helsinki testbed observations and model simulation. *Mon. Weather Rev.* **139**: 2876–2900.
- Keyser D, Anthes RA. 1982. The influence of planetary boundary layer physics on frontal structure in the Hoskins–Bretherton horizontal shear model. *J. Atmos. Sci.* **39**: 1783–1802.
- Keyser D, Pecnick MJ. 1985. A two-dimensional primitive equation model of frontogenesis forced by confluence and horizontal shear. *J. Atmos. Sci.*, **42**: 1259–1282.
- Martin JE. 1998. On the deformation term in the quasigeostrophic omega equation. *Mon. Weather Rev.* **126**: 2000–2007.
- Miller JE. 1948. On the concept of frontogenesis. *J. Meteorol.* **5**: 169–171.
- Montgomery MT, Farrell BF. 1991. Moist surface frontogenesis associated with interior potential vorticity anomalies in a semigeostrophic model. *J. Atmos. Sci.* **48**: 343–367.
- Novak DR, Colle BA, McTaggart-Cowan R. 2009. The role of moist processes in the formation and evolution of mesoscale snowbands within the comma head of northeast U.S. cyclones. *Mon. Weather Rev.* **137**: 2662–2686.
- Parker DJ, Thorpe AJ. 1995. The role of snow sublimation in frontogenesis. *Q. J. R. Meteorol. Soc.* **121**: 763–782.
- Pielke RA, Cotton WR, Walko RL, Tremback CJ, Lyons WA, Grasso LD, Nicholls ME, Moran MD, Wesley DA, Lee TJ, Copeland JH. 1992. A comprehensive meteorological modeling system: RAMS. *Meteorol. Atmos. Phys.* **49**: 69–91.
- Posselt DJ, Martin JE. 2004. The effect of latent heat release on the evolution of a warm occluded thermal structure. *Mon. Weather Rev.* **132**: 578–599.
- Reeves HD, Lackmann GM. 2004. An investigation of the influence of latent heat release on cold-frontal motion. *Mon. Weather Rev.* **132**: 2864–2881.
- Saleeby SM, Cotton WR. 2004. A large-droplet mode and prognostic number concentration of cloud droplets in the Colorado State University Regional Atmospheric Modeling System (RAMS). Part I: Module descriptions and supercell test simulations. *J. Appl. Meteorol.* **43**: 182–195.
- Saleeby SM, Cotton WR. 2007. A binned approach to cloud-droplet riming implemented in a bulk microphysics model. *J. Appl. Meteorol. Climatol.* **47**: 694–703.
- Szeto KK, Stewart RE. 1997. Effects of melting on frontogenesis. *J. Atmos. Sci.* **54**: 689–702.
- Thorpe AJ, Emanuel KA. 1985. Frontogenesis in the presence of small stability to slantwise convection. *J. Atmos. Sci.* **42**: 1810–1824.
- Van Delden A. 1999. The slope of isentropes constituting a frontal zone. *Tellus* **51A**: 603–611.
- Woods CP, Locatelli JD, and Stoelinga MT. 2008. The IMPROVE-1 Storm of 1–2 February 2001. Part IV: Precipitation enhancement across the melting layer. *J. Atmos. Sci.* **65**: 1087–1992.